

RESEARCH ARTICLE

Structure–function relationship during the early and long-term hydration of one-part alkali-activated slag

Teresa Liberto¹  | Maria Chiara Dalconi²  | Gregorio Dal Sasso³  |
Maurizio Bellotto⁴  | Agathe Robisson¹ 

¹Institute of Materials Technology, Building Physics and Construction Ecology, Faculty of Civil and Environmental Engineering, TU Wien, Vienna, Austria

²Department of Geosciences and Circe Centre, University of Padua, Padova, Italy

³Institute of Geosciences and Earth Resources, National Research Council of Italy, Padova, Italy

⁴Opigeo SRL, Grisignano di Zocco, Italy

Correspondence

Teresa Liberto, Institute of Materials Technology, Building Physics and Construction Ecology, Faculty of Civil and Environmental Engineering, TU Wien, Karlsplatz 13, Vienna 1040, Austria.
Email: teresa.liberto@tuwien.ac.at

Funding information

TU Wien Bibliothek; Österreichische Forschungsförderungsgesellschaft (FFG), Grant/Award Number: 870962

Abstract

Understanding the mechanisms controlling the early (fresh) and long-term (hardened) hydration of one-part alkali-activated slags (AAS) is key to extend their use as low CO₂ substitutes for ordinary Portland cement (OPC). Their “just add water” use makes them easier and less hazardous to manipulate than the more studied two-part ones. This is due to the absence of liquid alkaline activators, which are environmentally and energy demanding. In this work, numerous experimental techniques have been linked to obtain a comprehensive physico-chemical characterization of a one-part AAS activated with Na₂CO₃ and Ca(OH)₂ powders at several water to solid ratios (w/s). Calorimetry and pH/conductivity measurements describe the functioning of the activators immediately after contact with water. Early reactivity is characterized through in situ X-ray powder diffraction (XRPD) and small amplitude oscillatory shear (SAOS) rheology, which reveal a rapid precipitation of nanometric hydration products (nano-C-A-S-H), which results in a continuous increase in the paste cohesivity until setting. Moreover, SAOS shows that rejuvenating the paste by means of shearing (performed externally to the rheometer in this study) is enough to restore the initial cohesion (i.e., workability) for long time spans until setting occurs. The long-term hydration is characterized by ex situ XRPD on aged AAS pastes, in parallel with mechanical testing on AAS mortar. A correlation can be observed between the amount of nano-C-A-S-H and the increase in compressive strength. Overall, this formulation shows satisfactory fresh and solid properties, demonstrating suitability for low- and normal-strength applications.

KEYWORDS

AAS, nano-C-A-S-H, SAOS, sustainability, XRPD

This is an open access article under the terms of the [Creative Commons Attribution-NonCommercial-NoDerivs](https://creativecommons.org/licenses/by-nc-nd/4.0/) License, which permits use and distribution in any medium, provided the original work is properly cited, the use is non-commercial and no modifications or adaptations are made.

© 2023 The Authors. *Journal of the American Ceramic Society* published by Wiley Periodicals LLC on behalf of American Ceramic Society.

1 | INTRODUCTION

One of the many challenges of our time is the development of cementitious materials with low CO₂ emissions to reduce the enormous environmental impact related to the construction industry. Several effective and practically viable strategies have been developed to mitigate this impact by partially or completely replacing ordinary Portland cement (OPC) in the formulation of blended cements or alternative binders. Worth mentioning is the reduction in clinker content by substitution with calcined clays and limestone materials, which is promising for large-scale deployment.¹ On a local scale, attractive strategies include the formulation of OPC-free binders based on the alkali activation of suitable calcium/aluminosilicate precursors, mostly constituted of industrial by-products. Within a circular economy perspective, the use of industrial by-products in the formulation of alternative binders represents a sustainable opportunity to close the loop of the product lifecycle and promote an integrated zero-waste industrial system.^{2,3} Alkali-activated binders, and more specifically alkali-activated slags (AAS), are a possible alternative to OPC, potentially important when their precursors are locally available^{4,5} and cost-effective in terms of material supply chain and placement technology. It is frequently estimated that blast furnace slag availability will not increase in the western world in the next years. However, other metallurgical slags with a composition similar to blast furnace slag may be used where locally available⁶ or their synthetic analog may be efficiently produced from the widely available white ladle steel slag which is mostly landfilled today.⁷ In AAS, the cement clinker is totally substituted by a solid amorphous aluminosilicate (precursor), activated by an alkaline solution (two-part system) or by a dry alkaline powder or a salt with alkaline hydrolysis (one-part system).^{8–10} One-part AAS set and harden upon mixing with water, similar to OPC. These systems are less studied in the literature due to their often slow strength development compared to the two-part ones.⁵ However, one-part AAS pose less safety issues for workers and have a lower CO₂ impact than two-part ones, due to the absence of liquid (alkaline) solutions, which are usually corrosive, and energetically and environmentally demanding. Many AAS formulations have been proposed in recent decades.^{11–14} The activation of ground granulated blast furnace slag (GGBS) is classically done with sodium hydroxide (NaOH), silicate (Na₂SiO₃, Na₂Si₂O₅), sulfate (Na₂SO₄), or carbonate (Na₂CO₃).¹⁵ The latter solid activator is used mainly in combination with other liquid ones (i.e., sodium hydroxide or silicate),^{9,14,16–19} requiring the handling of hazardous solutions and reducing its advantages compared to the benefits mentioned above for the

one-part AAS. In few instances, only sodium carbonate activation is associated with other solid components to enhance hydration kinetics as well as fresh and hardened properties.^{20–24} Most of these studies report results on the formulation of one-part AAS, as a ready-to-use product, or on their mechanical strength development, while no investigation has been devoted to revealing the mechanism that controls the workability and reactivity of early age pastes. The chemistry of AAS is relatively well-understood¹³ and predicted by thermodynamic modeling.^{25–29} Calcium aluminosilicate hydrate (C-A-S-H) is the main hydration product of AAS, with a chemical composition and structure similar to that of C-S-H that forms in OPC but characterized by aluminum uptake.^{11,13,29,30} More precisely, C-S-H and C-A-S-H are nanocrystalline materials whose structures slightly differ in relation to the content of aluminum ions, which preferably replace silicon ions at the bridging sites of the silicate dreierketten chain.^{31,32} Similarly to OPC, the phase assemblages of hydrated AAS can be predicted on the basis of thermodynamic modeling starting from the chemical composition of the system, and graphically represented in the subternary CaO–Al₂O₃–SiO₂ phase diagram.^{13,33} Such thermodynamic modeling is also of great importance for predicting the long-term behavior of AAS, overcoming the lack of durability experiments.^{29,34} Parallel to thermodynamic modeling, long-term experimental characterization of hydrating AAS is generally carried out through X-ray diffraction (XRD), X-ray fluorescence (XRF), nuclear magnetic resonance (NMR) spectroscopy, scanning electron microscopy (SEM), calorimetry, thermogravimetric analysis (TGA), and compressive strength testing on solid prisms.^{22,35–39} As already mentioned, the early reactivity (i.e., first hours) of AAS pastes has been investigated less. Few studies deal with the characterization of the fresh properties of mainly two-part AAS pastes,^{40–42} focusing on their poor workability,^{43–45} whereas a recent study⁴⁶ follows the early reactivity of a slag paste activated with sodium silicate by rheology.

In this study, we focus on the formulation of a one-part AAS paste, based on GGBS as a precursor activated with sodium carbonate, along with calcium hydroxide (Ca(OH)₂). The hydration process and the chemical equilibria between the solids and the interstitial solution in this one-part system are markedly different from the two-part AAS activated with sodium silicate, mainly due to the different concentrations of silicate in solution. Despite the performance of this sustainable and chemically harmless formulation,⁴⁷ less attention has been paid to it. In fact, while this system has been industrially used in the past,^{12,48} it has only been recently and partially characterized.^{45,49} In particular, the roles of sodium carbonate and of the

interstitial solution composition, specifically carbonate ions, have been pointed out by Bernal et al.³⁸ and by Ke et al.³⁹ Here, we provide a novel multiscale approach to the characterization of the early and long-term hydration of this one-part AAS paste, linking its rheological and mechanical properties to structural and microstructural features. This has been achieved by combining, for the first time, several techniques that encompass different research fields, through real-time and ex situ measurements. A detailed characterization of hydration products in AAS pastes was obtained using synchrotron X-ray powder diffraction (S-XRPD) to identify minor and poorly crystalline phases. In addition, the early and long-term hydration products of the AAS paste (fresh and solid) were measured by laboratory in situ and ex situ XRPD. The pH and electrical conductivity of an AAS suspension were monitored for the first hours after contact with water to have an indirect measurement of the evolution of ionic concentration. Hydration of an AAS paste was followed for several hours with calorimetry and the Vicat apparatus. Small amplitude oscillatory shear (SAOS) rheology was used to measure the structural build-up of AAS pastes at different concentrations over time, as it is increasingly being done for OPC^{45,50–56} to monitor the chemical processes during its hydration (e.g., dissolution–precipitation mechanisms⁵⁷). Finally, mortar AAS prisms were prepared and tested at different curing times up to 28 days at several water to solid ratios (w/s). The combination of these techniques brings novelty to the understanding of this one-part formulation, clarifying the mechanisms responsible for the early and long-term hydration, and providing an interpretation of compelling performances in both initial reactivity and cohesion, setting time and solid mechanical properties. This multi-technique approach aims at linking the vast literature cited above on one-part AAS (mostly sodium carbonate based)^{9,10,14,17,18,20–24,38,39} to (i) the formation of hydrated phases and their structural and microstructural characteristics, (ii) the dissolution–precipitation processes (as determined by the pH and composition of the interstitial solution), and (iii) the influence of all these phenomena on the early macroscopic paste structuration and increase in elastic properties. The techniques used span from the well-established measurements of compressive strength, hydration calorimetry, and mineralogical phase identification and quantification by XRPD, to others that are less frequently reported in literature. Among these we may cite (i) SAOS measurements, which is gaining interest recently,^{45,50–56} (ii) interstitial solution pH and conductivity measurements, techniques scarcely applied despite being introduced in the 1980s,^{58–60} and (iii) S-XRPD, which can be fruitfully applied to research activities once the access to large-scale facilities is granted.⁶¹

2 | MATERIALS AND METHODS

This section describes in detail the formulation of our AAS and all the methodologies used to characterize its hydration process from the microscale to the macroscale. The same batch of AAS powder was used throughout the study. The mixing process and w/s are optimized for each specific test. More specifically, the paste needs to be fluid enough to be loaded in the capillary for S-XRPD. Similarly, the paste must be fluid and low absorbent for the Cu $K\alpha_{1,2}$ radiation of the laboratory in situ XRPD. On the contrary, SAOS rheological experiments have been performed at various w/s to investigate the effect of the solid volume fraction of the paste on the elastic characteristics. Various w/s have also been used for the Vicat and compressive strength measurements. Hydration calorimetry data have been measured at fixed w/s = 0.4 to enhance the heat release per unit mass of the paste. Finally, pH and electrical conductivity tests have been performed on a suspension with w/s = 3 to enable the reading of the measuring electrodes. The mixing procedures have also been adapted to each technique following standard procedures, where existing, as detailed below for each specific one.

2.1 | Alkali-activated slags

AAS consists of 91.5% ground and granulated blast-furnace slag GGBS (Ecozem, $\rho \approx 2.9 \text{ g/cm}^3$), 5% sodium carbonate Na_2CO_3 (VWR, $\rho = 2.5 \text{ g/cm}^3$), and 3.5% calcium hydroxide $\text{Ca}(\text{OH})_2$ (VWR, $\rho = 2.2 \text{ g/cm}^3$).⁴⁵ For this one-part formulation ($\rho_{\text{AAS}} \approx 2.9 \text{ g/cm}^3$), two solid activators (Na_2CO_3 and $\text{Ca}(\text{OH})_2$) were chosen to further reduce the environmental impact of AAS compared to the more energy-intensive and hazardous liquid ones (two-part). The addition of Na_2CO_3 and $\text{Ca}(\text{OH})_2$ in equal stoichiometric amounts optimizes both the early setting and the long-term strength.^{12,49} Sodium carbonate is, in fact, routinely used in AAS as a solid activator, while calcium hydroxide plays the role of a setting and hardening accelerator.³⁸ Hydrate precipitation and AAS setting start when all carbonate ions in solution, CO_3^{2-} , are consumed by reacting with calcium ions, Ca^{2+} , and precipitate as CaCO_3 . Calcium ions come from the dissolution of the slag or from additional calcium-bearing soluble phases (i.e., $\text{Ca}(\text{OH})_2$).

The particle size distribution of our commercial GGBS was measured with a dry particle size analyzer (Better-sizer SD). Three measurements were made, resulting in $D_{10} = 1.464 \pm 0.015 \mu\text{m}$, $D_{50} = 9.30 \pm 0.15 \mu\text{m}$, and $D_{90} = 30.79 \pm 0.42 \mu\text{m}$. The exact chemical composition of our GGBS was determined by XRF and reported in

Figure S1. AAS suspensions or pastes are made by mixing distilled water and the solid dry powder portion (91.5 wt% GGBS, 5 wt% Na_2CO_3 , 3.5 wt% $\text{Ca}(\text{OH})_2$) at several w/s, depending on the technique used.

2.2 | Synchrotron X-ray powder diffraction

A synchrotron XRPD experiment was performed at the X04SA-MS beamline of the Swiss Light Source (Paul Scherrer Institut, Villigen, CH) to obtain accurate information on the phases forming during the early hydration of AAS paste, taking advantage of (i) the higher brilliance and collimation of the X-ray radiation with respect to laboratory sources, providing high-quality data at high resolution, and (ii) the tunable beam energy, enabling the selection of the most suitable wavelength to explore the desired Q -range in the scattering pattern (vide infra).^{62,63} The GGBS was loaded in a 0.5 mm diameter glass capillary and measured as reference material before activation. The AAS paste was prepared by mixing the powder with distilled water at w/s = 0.5 and then loaded into a 0.5 mm diameter glass capillary and measured at different times (0.4, 17, 33, 46, and 76 h) to evaluate the evolution of the system in terms of phase assemblage. S-XRPD data were collected in transmission mode in the 2θ range of 2° – 120° using a single-photon counting silicon microstrip MYTHEN II detector. The beam energy was set at 22 keV, and the operational wavelength $\lambda = 0.56456 \text{ \AA}$, determined by measuring a silicon powder standard sample (NIST 640c). Separate scattering measurements of the air and empty capillary were also performed. The transmission coefficient of the samples was experimentally determined by measuring direct and transmitted beams, whereas that of the glass capillary was calculated from the certified composition and the wall thickness of the capillary. Raw data were corrected for systematic errors and absorption effects; the extra-sample contributions to the scattering pattern (i.e., the scattering from the capillary and the sample environment) were subtracted, thus obtaining the reduced S-XRPD data constituted by the sole sample scattering pattern.

2.3 | Laboratory X-ray powder diffraction

The early hydration of AAS pastes was characterized through in situ laboratory XRPD measurements in focusing transmission geometry. The AAS suspension was prepared by mixing the dry powder with distilled water at w/s = 0.6, in order to obtain a paste with high fluidity. After mixing for 30 seconds with an orbital shaker, approx-

imately 0.2 g of paste was inserted between two films of low-density polyethylene and mounted on a 35 mm diameter sample holder. Sample thickness is a critical parameter for measurements in transmission geometry, and, to avoid absorption-related issues, the specimen was prepared using a small amount of material. The confinement of the paste between two polyethylene films prevented carbonation or desiccation of the paste. The measurements were carried out under isothermal conditions at 23°C , maintaining the sample spinning during data acquisition. It is worth mentioning that when measuring pastes or suspensions, the symmetrical transmission geometry has definite advantages over the classical Bragg–Brentano parafocusing reflection geometry. First, sealing a thin paste layer between two polyethylene foils avoids any sedimentation and inhomogeneity of the sample (which is almost unavoidable in the thick horizontal samples in the Bragg–Brentano geometry). Additionally, when the measurement is in transmission, geometrical aberrations related to sample displacement are minimized, the irradiated area is better defined (particularly in the crucial low-angle region⁶⁴), and less interfering peaks of polyethylene film are detected. In situ diffraction measurements were performed with a Panalytical X'Pert PRO MPD diffractometer using a focusing transmission flat sample geometry. The diffractometer was equipped with a Cu X-ray tube (Cu $K\alpha_{1,2}$ radiation), an elliptical focusing X-ray mirror and the PIXcel detector (active detecting length $3.3^\circ 2\theta$). This experimental setup enabled fast diffraction measurements that covered a wide 2θ range. Diffraction patterns were continuously recorded in the 3° – $66^\circ 2\theta$ range starting at 10 min up to 7.5 h of hydration time. The measuring time of a single diffraction pattern was 20 min.

The phase composition of AAS pastes at curing times of 1, 7, 14, and 150 days were characterized through ex situ diffraction measurements. In this case, AAS paste was prepared by mixing dry powder with distilled water using w/s = 0.4, poured into polyethylene containers and cured at $22^\circ\text{C} (\pm 2^\circ\text{C})$ and a relative humidity of 99%. At selected curing times, a portion of the solid sample was ground, hydration was stopped by immersion in ethanol, and the dried powders obtained were prepared for diffraction measurements. A known amount (10 wt%) of internal standard zincite (Baker™ ZnO) was added to the powder samples, as required for quantifying the amorphous content. Ex situ measurements were performed with the diffractometer in Bragg–Brentano reflection geometry, using a fixed divergence slit (0.25° aperture) and acquiring diffraction data in the 5° – $90^\circ 2\theta$ range, step size $0.026^\circ 2\theta$, equivalent time per step of 117 s. Quantitative phase analysis of AAS pastes was obtained using the Rietveld full-profile fitting approach. Topas v 2.1 software⁶⁵ was used for

Rietveld refinements, applying the fundamental parameters approach to simulate the instrumental contribution to line broadening. The PONKCS method⁶⁶ was used to quantify C-A-S-H in the hydrated pastes, whereas the amorphous content, mainly related to the unreacted slag, was calculated using the internal standard method.

2.4 | pH/conductivity

The pH and conductivity of an AAS suspension, at $w/s = 3$, were measured together through a pH/cond-meter (SevenCompact pH/cond S213 Mettler Toledo) with electrodes optimized for highly alkaline solutions. The pH electrode was calibrated with buffer solutions at pH 7.00, 9.21, 10.00, and 12.45. The electrical conductivity electrode was calibrated with a solution at 12.88 mS/cm, and the measuring range was checked with a saturated NaCl solution. Both probes were inserted into the suspension immediately after mixing the AAS powder with distilled water by hand. The measurement was carried out for 4 h under continuous magnetic stirring.

2.5 | Calorimetry

Calorimetry tests were carried out on an AAS paste at $w/s = 0.4$ in a custom-built semiadiabatic (isoperibolic) multichannel calorimeter equipped with type K (nickel–chromium/nickel–alumel) thermocouples (OMEGA). Semiadiabatic (isoperibolic) calorimetry is a well-established technique,^{67,68} routinely used to study cement hydration.^{69,70} Moreover, it constitutes the basis of the European Standard EN 196-9:2010. Performing the measurements in the semiadiabatic mode approaches the real-life cement hydration conditions more closely compared to the isothermal mode. The 50 mL paste is obtained by mixing distilled water with AAS powder using an overhead stirrer (IKA) for three minutes at the maximum speed (800 rpm). Immediately after mixing, the paste was inserted into an isolated container and placed inside an insulated chamber. Then, two thermocouples were inserted to measure both the sample and chamber temperatures.

2.6 | Small oscillatory rheology

SAOS rheological measurements were performed on AAS pastes at $w/s = 0.4, 0.5$, and 0.6 ($\Phi \simeq 0.46, 0.41$, and 0.36 , respectively) using a torque-controlled rotational rheometer (MCR 302, Anton Paar) equipped with a serrated plate-plate geometry, with an upper diameter of 25 mm

(PP25/P2) and a lower one of 50 mm. The gap between plates was optimized for each paste in a range between 1.50 and 2.55 mm to minimize the disruption of the paste upon loading and to avoid wall slip.^{45,71} Homogeneous 10 mL paste samples were obtained by dispersing AAS powder in distilled water using an Ultra Turrax mixer (IKA) at the maximum velocity (6000 rpm) for 3 min. This high intensity mixing is necessary for a complete mechanical destructure (i.e., fluidization) of the paste, allowing both the reproducibility and the correct interpretation of the results. Immediately after mixing, the paste was loaded onto the rheometer, the final contact gap was reached, the moisture chamber was placed (to avoid evaporation) and the test started. This process took ca. 60–90 s.

To measure the structural buildup of the AAS pastes, preserving the existing microscopic structure, a small amplitude oscillatory deformation was imposed in the linear-viscoelastic regime (LVE) of the paste, independently measured at all concentrations explored in this work, as specified in a previous publication.⁴⁵ For all concentrations, the pastes showed an attractive gel-like behavior, where the storage modulus G' was higher than the loss one G'' .⁷¹

Thus, an amplitude oscillatory deformation of $\gamma = 0.0005\%$ (within the LVE) at $f = 1$ Hz was imposed for 1 h.^{45,71} The choice of 1 Hz frequency was arbitrarily made, as the results obtained on cementitious pastes were reported to be unaffected by frequency.^{45,50,51,53,54} The temperature was kept constant at 20°C. The evolution of the normal force was monitored to confirm the contact between the upper plate and the paste. This measurement set the temporal limit of the test to one hour for the most concentrated paste, showing at this time a discontinuity due to the partial detachment of the upper plate, probably related to early hydration shrinkage. To overcome this limitation, multiple distinct samples (i.e., batches) were prepared, for each concentration, at a similar initial time (i.e., 15 min apart considering the unloading, cleaning and loading process between different samples). All samples were prepared exactly the same way with the same volume. For each concentration, the samples were then tested fresh and every hour since preparation. The aging then occurred outside the rheometer, and all the aged samples were remixed immediately before loading for three minutes at the maximum velocity (as in the preparation step). The duration of the test and therefore the number of samples for each concentration was dictated by their ability to exhibit a viscous fluid behavior and was a function of Φ , as described below:

- at $w/s = 0.4$ ($\Phi \simeq 0.46$), three samples were tested: fresh, after 1 h, and after 2 h from the preparation (i.e., overall testing time 3 h);

- at $w/s = 0.5$ ($\Phi \approx 0.41$), four samples were tested: fresh, after 1 h, after 2 h, and after 3 h from the preparation (i.e., overall testing time 4 h);
- at $w/s = 0.6$ ($\Phi \approx 0.36$), five samples were tested: fresh, after 1 h, after 2 h, after 3 h, and after 4 h from the preparation (i.e., overall testing time 5 h).

As expected, the higher the w/s (the lower the Φ), the larger the testing time window on the rheometer. Each concentration was tested until the paste showed a substantial decrease in workability (due to the hydration progress), being too stiff to be tested by the rheometer (i.e., torque limit). For each concentration, three sets of tests were performed to assess the reproducibility of the results.

2.7 | Vicat

The setting times of the two extreme concentrations of the AAS paste, $w/s = 0.4$ and 0.6 , were measured by the automatic Vicat apparatus (Vicomatic, CONTROLS). Samples with a volume of 250 mL were prepared by dispersing the AAS powder in distilled water with the aid of an overhead stirrer (IKA) for three minutes at maximum speed (800 rpm). As specified in the norm EN 196-3, the paste was placed in the mold immediately after the preparation inside a container that was then filled with water until ca. 1 mm above the upper surface of the sample (to avoid drying). Vicat tests start with a needle penetration depth of 40 mm and stop after a certain number of drops (44) dictated by the upper surface area of the mold. Then, an initial delay time and the time between the drops were set for both concentrations to cover most of the setting window. Two tests were repeated for each concentration to verify the reproducibility of the results.

2.8 | Mechanical testing

The mechanical compressive strength of the solid AAS mortar was also measured with a Zwick Roell machine (Z250). Prisms of $2 \times 2 \times 8 \text{ cm}^3$ were prepared by mixing AAS powder with 30% in volume of standard sand (1–2 mm) and tap or distilled water at different w/s (i.e., 0.35–0.50) and tested at different curing times (i.e., from 1 to 28 days). An overhead stirrer (IKA) was used with the following mixing procedure: 1 min at low speed (200 rpm) to homogenize sand, AAS powder, and water, then 1 min at high speed (800 rpm), a short stop to remove the material from the wall and finally another minute at high speed. The AAS mortar prisms were then placed in the molds and stored in a climate chamber at 20°C and 65% humidity.

3 | RESULTS AND DISCUSSION

This section is organized into three parts: the first provides a general description of the phase assemblage that develops during the hydration of the AAS, and the second and third show and discuss the results obtained with the various techniques already presented and aim at describing the initial hydration mechanisms of the AAS paste and the long-term evolution of the system, respectively.

3.1 | Phase assemblage via S-XRPD

The S-XRPD pattern of GGBS (Figure S2) shows broad humps characteristic of an amorphous material. The high-resolution S-XRPD data enable the detection of minor amounts of crystalline phases (i.e., calcite, aragonite, periclase, $\beta\text{-C}_2\text{S}$ and vaterite), most of which are below the detection limit of the laboratory XRPD analysis. These phases do not participate in the early hydration stage of the AAS paste, as their (weak) characteristic peaks are also detectable in the S-XRPD measurements performed on the AAS paste at different maturation times. S-XRPD data are reported in the Q range, where $Q = 4\pi \cdot \sin(\theta)/\lambda$, with θ being half of the scattering angle 2θ , $\lambda = 0.56456 \text{ \AA}$. As shown in Figure 1, the AAS paste measured just after mixing (0.4 h) shows a scattering pattern dominated by the signal of the GGBS together with the newly precipitated calcite (main peak at ca. 2.07 \AA^{-1}) and a minor portlandite residue (the amount of which is reasonably below the detection limit of laboratory XRPD).

At 33 h after mixing, a broad peak starts to be visible at ca. 0.82 \AA^{-1} (corresponding to a d -spacing of 7.66 \AA), and sharpens at higher maturation times, suggesting the precipitation of a nanosized AFm phase. These AFm phases have a layered structure composed of calcium aluminate layers stacking along one direction and, in the interlayer space, different anions (OH^- , SO_4^{2-} , CO_3^{2-}) can be hosted, thus allowing for variability in chemical composition. The detected peaks of AFm phases are possibly assigned to monocarboaluminate (CO_3^{2-} -AFm) or to a hydrotalcite-type phase, a layered structure composed of magnesium aluminate layers.⁷² Given the structural similarity among the AFm phases and the hydrotalcite-type phases, it is not straightforward to distinguish the two groups of phases by XRPD if only a few reflections are observed. From now on, both the CO_3^{2-} -AFm phase and hydrotalcite-type phase are globally indicated as AFm phases. The progressive broadening of the peak at 2.07 Q (Å^{-1}) (d -spacing of 3.04 \AA) and the subsequent appearance of a shoulder at lower Q with maturation time have been attributed to the nucleation and growth of C-A-S-H

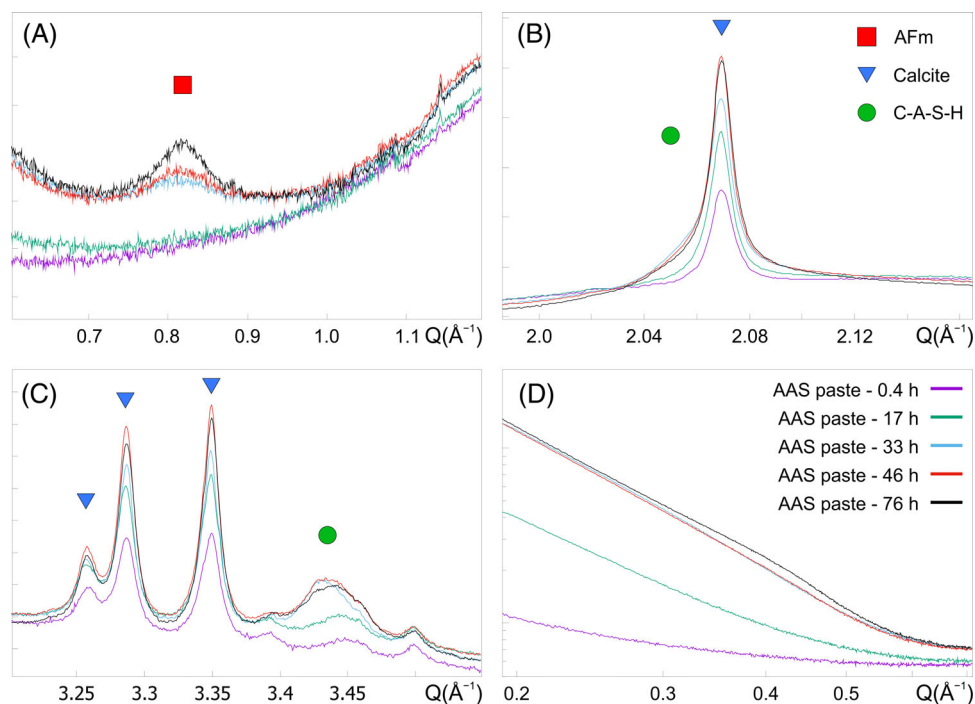


FIGURE 1 Details of the synchrotron X-ray powder diffraction (S-XRPD) patterns of the $w/s = 0.5$ alkali-activated slag (AAS) paste at different maturation times (0.4, 17, 33, 46, and 76 h). S-XRPD patterns show (A) the progressive precipitation of nanosized AFm (□) with peak position at ca. 0.82 \AA^{-1} ; (B and C) the progressive nucleation and growth of nano-calcium aluminosilicate hydrate (C-A-S-H) (○) highlighted by the broadening of the superimposed calcite (▽) peak at ca. 2.07 \AA^{-1} and the increasing shoulder at 2.05 \AA^{-1} and by the occurrence of the peak at ca. 3.43 \AA^{-1} ; (D) the increase in intensity in the low- Q region (plotted on a log-log scale) and the beginning of nano-C-A-S-H structuration at 76 h.

nanoparticles, for which the main diffraction peak partially overlaps that of calcite. The characteristic pattern features of developing C-A-S-H (Figure S3) are also visible at ca. 3.43 \AA^{-1} (d -spacing of 1.83 \AA) (Figure 1C).⁷³ The assemblage of hydration products detected here is in agreement with that observed in similar one-part AAS formulations.²² Notably, the S-XRPD experimental setup allows one to record a low- Q scattering pattern, from 0.19 to ca. 0.50 \AA^{-1} (Figure 1D), corresponding to the high- Q region of a small-angle X-ray scattering (SAXS) pattern, namely the upper limit of the Porod region.⁷⁴

The scattering intensity in this low- Q range is dominated by the typical SAXS signal generated by small (nano-sized) scattering entities. The conventional SAXS signal can be described by considering the different scattering contrast of such entities with respect to the surrounding media, their volume fraction, the form factor $P(q)$ describing the size and shape of the scattering object, and the structure factor $S(q)$ describing the interparticle interaction. However, in this case, the limited SAXS region accessible by this experimental setup prevents the full characterization of such entities and the theoretical modeling of a partial SAXS signal. Nevertheless, the increasing scattering intensity at increasing maturation

time provides valuable (although qualitative) information on the evolution of the system, suggesting the progressive nucleation and growth of nanostructured phases, for which both the volume fraction and size reasonably contribute to the recorded signal. This low- Q signal may result from the joint contribution of different nanostructured phases, such as newly precipitated AFm and C-A-S-H. Interestingly, the AAS paste at 76 h after mixing shows a very broad hump at ca. 0.4 \AA^{-1} (Figure 1D), which may be more reasonably attributed to a Bragg peak rather than a proper SAXS feature, corresponding to a d spacing of ca. 16 \AA and compatible with an early-precipitated C-A-S-H with a tobermorite-like structure. The characteristic features of C-A-S-H, highlighted in the S-XRPD pattern at higher Q and previously discussed, further support this.

3.2 | Early hydration properties (<1 day)

In situ XRPD, pH/conductivity, calorimetry, SAOS, and Vicat techniques are used to complement the microstructure understanding provided by S-XRPD, and bridge the scales between atomic interactions and macroscopic behavior.

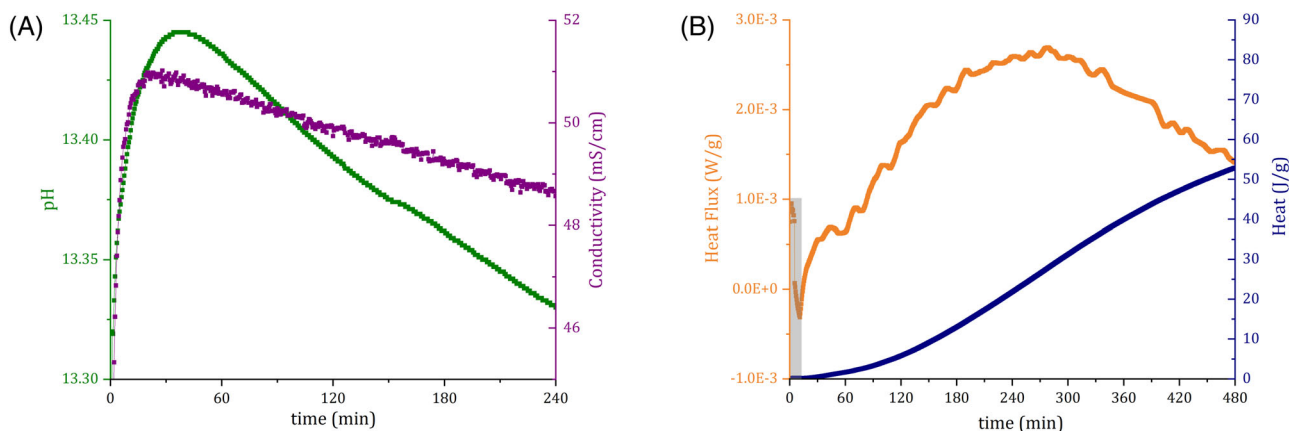
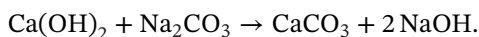


FIGURE 2 (A) pH/conductivity measurements over time for an alkali-activated slag (AAS) suspension at $w/s = 3$. (B) Heat flux and cumulative heat of hydration of an AAS paste at $w/s = 0.4$, obtained from semiadiabatic calorimetry measurement over time. Here, only the first 8 h are shown. The complete curve is reported in Figure S4.

3.2.1 | Early CaCO_3 precipitation

The pH and conductivity of an AAS suspension ($w/s = 3$) were measured simultaneously over 4 h under continuous magnetic stirring. As shown in Figure 2A, the evolution of pH and conductivity with time shows similar trends, with an initial increase followed by a decrease in time, starting in the first hour. Calorimetry instead, allows us to follow the heat of hydration developed from an AAS paste at $w/s = 0.4$, as shown (for the first 8 h) in Figure 2B. The rate of heat evolution and the cumulative heat of hydration were calculated based on the mass of the fresh sample ($w/s = 0.4$). The curve shows an initial endothermic peak (ca. 15 min, gray area). The main peak of hydration begins in the first couple of hours of testing, reaching its maximum around 4 h, and plateauing after around 20 h (Figure S4). As shown in Figure 2A, the maximum conductivity is reached after about 15 min, corresponding to the maximum calcium carbonate (CaCO_3) supersaturation and precipitation rate, and is attributed to the dissolution of the soluble activators. The subsequent decrease in conductivity is linked to continuing precipitation of CaCO_3 and possibly of the hydrated phases. The maximum pH is reached after about 30 min suggesting that CaCO_3 precipitation from the activators is completed within this time frame, according to the reaction:



The subsequent sharp decrease in pH values after 60 min denotes that hydroxylated solid phases precipitate quickly (also monitored by low-angle scattering in Figure 3 and Figure 4A), showing an accelerated increase after approximately 60 min. The maxima of electrical conductivity and pH do not coincide, although hydroxyls are the most significant contributors to the pore solution conductivity.⁷⁵

They are, in fact, related to different phenomena, the maximum CaCO_3 supersaturation and the completion of CaCO_3 precipitation, respectively. Additionally, the interactions between ions, solvent molecules, and ion pairs that occur in concentrated solutions affect the ionic mobility and change the effective ionic radii, causing conductivity to decrease while pH continues to increase.⁷⁶

In the same time frame of the conductivity measurements (i.e., 15 min), the heat flux in Figure 2B shows an endothermic peak (gray area), probably associated with the CaCO_3 precipitation whose enthalpy is negative, and is driven by its entropic contribution.⁷⁷ This hypothesis is supported by the heat value of 1.70 J/g calculated by the integral underneath the negative area of the heat flux (gray area, Figure 2B). This value is comparable to the theoretical one (2.49 J/g of paste) for the precipitation of CaCO_3 from the activators. The trend of heat flux supports the interpretation of the pH/conductivity curves, indicating that calcium carbonate precipitation from activators is limited to the first 30 min of hydration. The main peak related to the heat of hydration is a sum of the individual enthalpies of the reaction and takes into account both the heat released by precipitation of hydration products (nucleation) and their growth over time.⁷⁸ Therefore, the timing of the main peak cannot be directly related to the other techniques described below.

Overall, a rapid dissolution of solid activators brings an increase in pH and in the precipitation of CaCO_3 (ca. 30 min). An early age hydration peak is then visible for the AAS paste (ca. 250 min), linked to both nucleation and growth of hydration products.

3.2.2 | Early C-A-S-H formation and setting

In situ XRPD measurements were conducted to continuously monitor the phase evolution of the AAS paste at

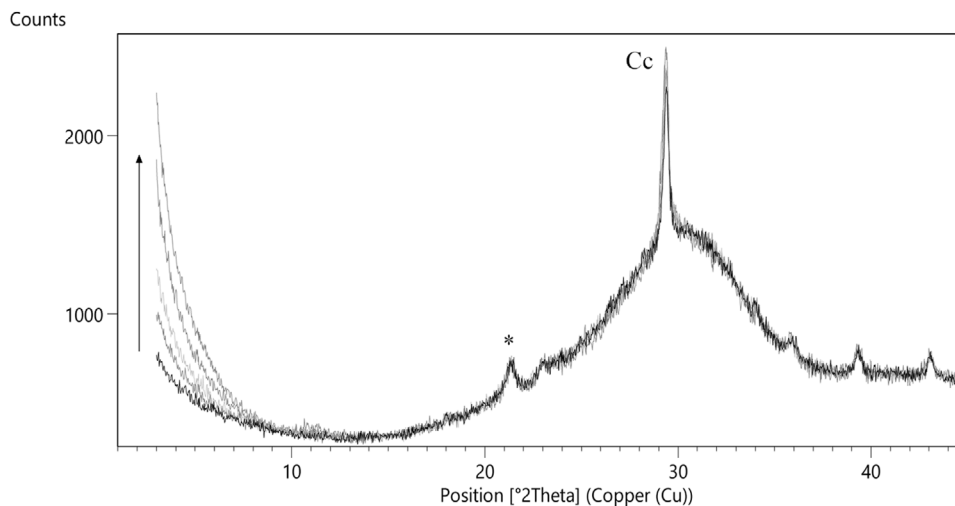


FIGURE 3 Selected in situ diffraction patterns of the alkali-activated slag (AAS) paste at $w/s = 0.6$ during the first 450 min of hydration. Cc: calcite; *: peak related to polyethylene film used as sample holder.

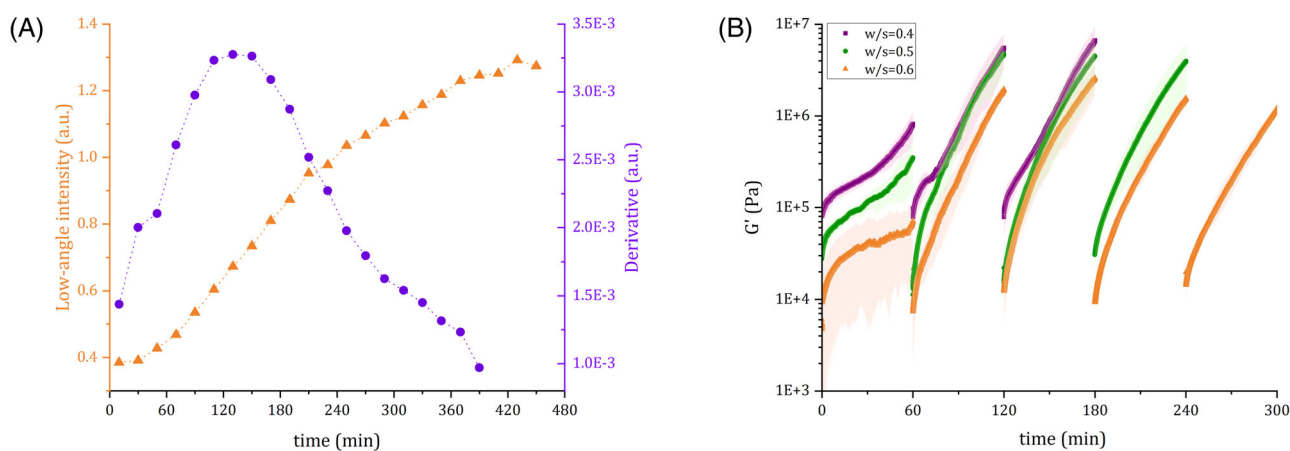


FIGURE 4 (A) Scattering intensity in the 3° – 7° 2θ range (i.e., low angle) as a function of the hydration time of an alkali-activated slag (AAS) paste at $w/s = 0.6$. (B) Structuration ($G'(t)$) of AAS pastes at different w/s over time.

$w/s = 0.6$ during the very early stages of hydration. Figure 3 shows the diffraction patterns starting from 10 min up to 450 min after mixing with water. The wide hump centered at $30^\circ 2\theta$, which is related to the slag contribution, does not exhibit any perceptible decrease. The only crystalline phase detected is calcite, and no diffraction peaks of calcium hydroxide (or portlandite, $\text{Ca}(\text{OH})_2$ or CH) and sodium carbonate (or natrite, Na_2CO_3 or sc) are observed indicating that these phases dissolved (or are below the detection limit of the technique) during the early minutes of mixing with water (as observed in the pH and calorimetry measurements). The low-angle region between the 3° and $7^\circ 2\theta$ interval (corresponding to a Q range of 0.21 – 0.49 \AA^{-1} using the $\text{Cu K}\alpha_1$ radiation) shows a marked increase as a function of hydration time. The kinetics of the paste evolution can be described by the increase in the low-angle intensity as a function of time. The low-angle intensity was

quantified by fitting the data in the 3° – $7^\circ 2\theta$ range using a split Pearson-VII function and keeping it fixed at a minimum value the full-width-half-maximum of the left side of the peak (i.e., $3.05^\circ 2\theta$). The refined peak area was used as a measure of the small-angle intensity, which is plotted with its derivative versus time in Figure 4A.

As shown in Figure 4B, *rheological tests* were performed for three w/s : 0.4, 0.5, and 0.6, a range for which the paste shows a gel-like behavior (i.e., $G' > G''$). As a quick reminder, for each w/s , the AAS pastes were prepared in several batches to gradually age outside the rheometer (to overcome the maximal duration of the experiment of 1 h). Each sample was remixed before being loaded onto the rheometer. In Figure 4B the evolution of G' over time is plotted for each of these samples at different aging times (i.e., every structuration hour represents a separate experiment).

The choice of plotting the three w/s together over time as a single experiment intends to give a general picture of the evolution of the properties of the three concentrations over time. Each w/s has a different maximum testing time, which increases when the paste is diluted (as expected). In particular, at w/s = 0.4 ($\Phi \simeq 0.46$), three batches were prepared and tested fresh, after 1 h, and after 2 h from the preparation. The overall testing time was then 3 h. At w/s = 0.5 ($\Phi \simeq 0.41$), one additional hour was explored with an overall testing time of 4 h. Then, at w/s = 0.6 ($\Phi \simeq 0.36$) another hour was gained, for a total experimental time of 5 h.

The low-angle scattering intensity (Figure 4A) shows a limited increase over the first 60 min, followed by a more pronounced increase until about 120 min, where the derivative shows a maximum. The rate of increase then reduces until 450 min, the end of the experiment. Considering a constant contribution from the extra-sample scattering (e.g., sample holder, air) within the in situ experiment, the increasing intensity in the low-angle region indicates the development of nanostructured scattering entities. This can be reasonably related to the incipient formation of hydration products that are still lacking long-range atomic ordering (i.e., nano-C-A-S-H, nano-AFm) at this early stage of hydration. This is further supported by the S-XRPD measurements performed just after mixing and after 17 h, for which the increase in intensity in the low-angle region is not paralleled by detectable Bragg features of newly precipitated crystalline phases, whereas the nano-C-A-S-H and AFm phases are clearly detectable at a longer maturation time, when the structural order and size of the nanocrystalline domains increase. This experiment fills in the time gap before the S-XRPD measurement at 17 h, showing the rapid development of nanostructured phases. In general, the trend shown by XRPD reflects the hydration kinetics and is consistent with the variation in pH/conductivity and with the rheological values shown in Figure 4B and discussed below.

For all three concentrations, the data describe the progressive increase in storage modulus G' (stiffening) of the pastes over time (at rest), which seems to be slower for the first hour compared to the successive ones. In light of the XRPD results, a qualitative interpretation of the rheological data may be performed by looking at the normalized (between 0 and 1) trends of G' , calculated as $[G'(t) - G'(t_0)]/[G'(t_{\max}) - G'(t_0)]$, with $G'(t_0)$ being the storage modulus at the beginning of the step and $G'(t_{\max})$ being the storage modulus at the end of the step, as reported in Figure 5. This normalization enhances, for the three concentrations, the concavity of the first ~30/60 min curves versus the convexity of the successive ones. The initial period can be understood through soft gel theory,⁷⁹ which attributes the growth of G' to the reorganization of particles and not to the small amount of precipitated hydration

products (slow kinetics). When the curves begin to have a convex trend, the growth of G' cannot be explained along the same lines and may be attributed to a large increase in surface area related to the substantial precipitation of nanostructured hydrated phases (i.e., nano-C-A-S-H) and the progressive increase in contact between them⁸⁰ (fast kinetics). This description can be validated for the w/s = 0.6 with the results from in situ XRPD (Figure 4A). Considering that the evolution of G' is related to the rate of nano-C-A-S-H precipitation, a parallel between the in situ XRPD and the rheology can be made. Indeed, looking at the derivative of the intensity of the low-angle signal (diffraction data, Figure 4A), the maximum precipitation rate of nano-C-A-S-H occurs between 1 and 3 h, which also corresponds to the maximum G' value. Looking at Figure 4B, we can also observe that the storage modulus, for each of the three w/s after external remixing, nearly returns to its initial value G' of each fresh paste. This suggests that the remixing brings the cohesion to the same initial state for the entire testing period (different for each w/s). After that period, the structuration is no longer reversible, and the workability loss is significant (i.e., rheometer testing is not possible).

To verify whether the time window obtained by SAOS matches the setting time, Vicat tests were performed for the two extreme concentrations, w/s = 0.4 and 0.6. Here, the needle penetration depth was measured over time and the results of two distinct tests (for each w/s) are shown in Figure 6. For these tests, the initial setting time is arbitrarily taken when the slope of the curves changes, roughly defined by a vertical dark pink line in Figure 6. This time is similar to the one defined by the norm EN 196-3 (i.e., penetration depth of around 34 ± 3 mm). In the same figure, the overall rheological testing time is highlighted in pink for both concentrations. In the AAS pastes the setting starts at ca. 90 min for w/s = 0.4 and ca. 210 min for w/s = 0.6. The range within which rheological measurements are possible is ca. 180 min for w/s = 0.4 and ca. 300 min for w/s = 0.6, which corresponds to the time when the lower plateau of the Vicat curves begins. The initial setting point for the pastes (at both w/s) occurs at ca. 90 min before their loss of workability (~end of setting). When comparing rheology and Vicat, we should remember that the protocols of the two techniques are different. In the Vicat test, the paste is at rest during the whole time of the experiment (420 min). In rheology, on the other hand, the paste is remixed and loaded every hour. However, these results suggest that rheology is capable of measuring AAS pastes until the needle penetration depth is strongly reduced to a penetration depth of less than 5 mm. The parallel made between in situ XRPD and rheology for w/s = 0.6 can also be validated by Vicat. After ca. 180 min, the precipitation rate of nano-C-A-S-H decreases as shown by SAOS and XRPD measurements (Figure 4). This amount of

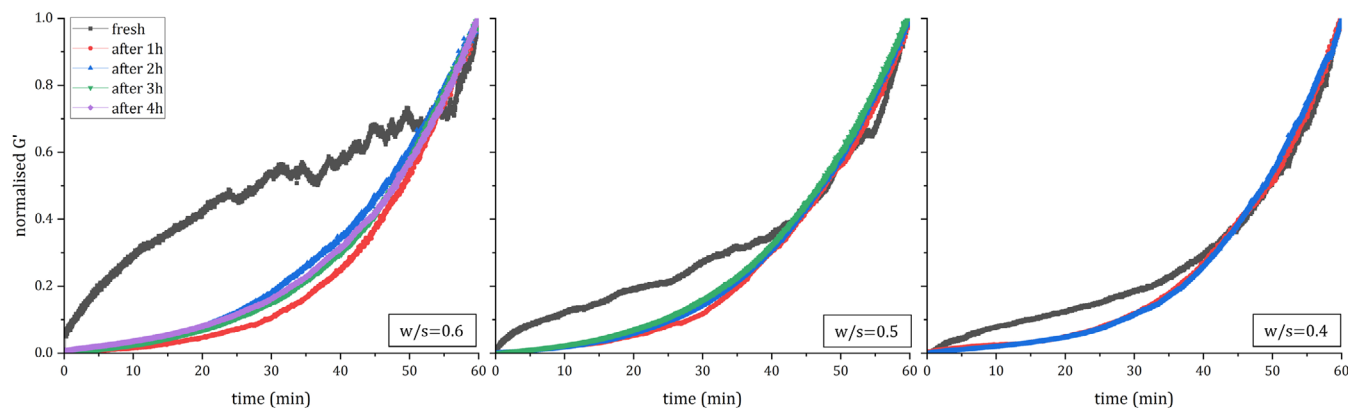


FIGURE 5 Normalized storage modulus G' as a function of time for the three w/s (from left to right 0.6, 0.5, 0.4).

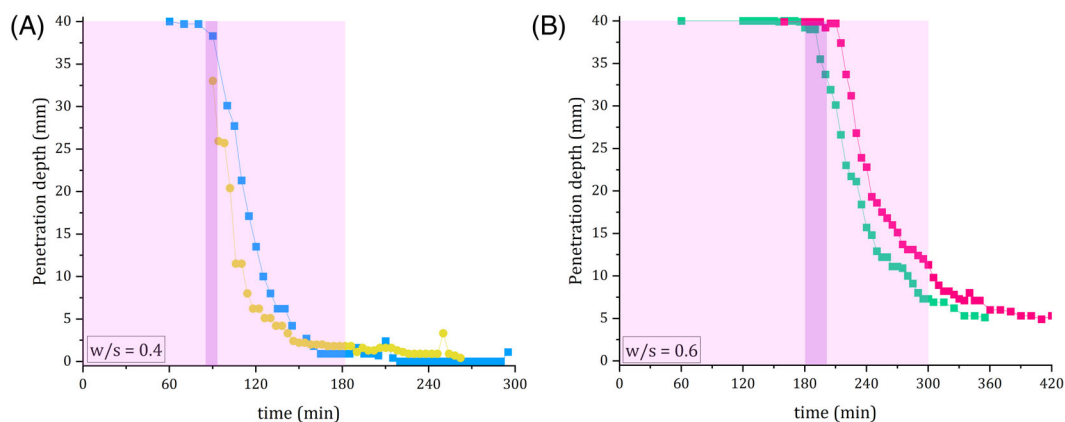


FIGURE 6 Vicat setting time for the two extreme water to solid ratios (w/s) of 0.4 (A) and 0.6 (B). The vertical dark pink line roughly defines the start of the setting. The pink area corresponds to the overall rheology testing time for the two concentrations.

precipitated nano-C-A-S-H determines a substantial loss of workability toward the start of the setting.

In summary, all these techniques suggest the presence of early hydration products (i.e., nano-C-A-S-H) whose precipitation rate increases $\sim 30/60$ min after contact with water (depending on the w/s), affecting the available surface area and the contact between the nanostructured hydrated phase, and consequently the macroscopic behavior of AAS pastes. These results show a rather fast development of early reactivity of the AAS paste, never measured before for systems activated by Na_2CO_3 .³⁸ Additionally, the workability of our one-part AAS can span from 3 to 5 h depending on the w/s , showing a similar initial cohesivity once remixed.

3.3 | Long-term properties (>1 day)

In this section, the long-term properties of AAS are studied via ex situ XRPD and mechanical testing. Ex situ laboratory XRPD measurements (supported by S-XRPD analysis)

were carried out on pulverized aged AAS pastes ($w/s = 0.4$) to characterize their long-term hydration products. The diffraction pattern of the starting AAS dry powder is shown in Figure 7A, while those of the pulverized aged AAS pastes after 1, 7, 14, and 150 days of curing time are shown in Figure 7B. As already observed by S-XRPD, the pattern of the initial AAS powder is dominated by a wide hump related to the contribution of amorphous slag, whereas the detected crystalline phases are a minor amount of calcite (Cc) and intentionally added portlandite (CH) and sodium carbonate (sc). In the patterns of the pulverized aged AAS pastes instead, diffraction peaks are assigned to AFm phases, calcite and nano-C-A-S-H. As already mentioned in the early hydration section, C-A-S-H is a poorly crystalline nano-phase and its diffraction contribution (detectable using a laboratory diffractometer) is limited to large peaks at $7^\circ 2\theta$ (d -spacing of 12.6 Å), at 29° – $30^\circ 2\theta$ (d -spacing of 3.0 Å, overlapped to calcite 104 reflection), and a weak peak at $50^\circ 2\theta$ (d -spacing of 1.83 Å), as shown in Figure 7B.⁸¹ The same diffraction features were also observed in the S-XRPD pattern of a pure C-A-S-H sample

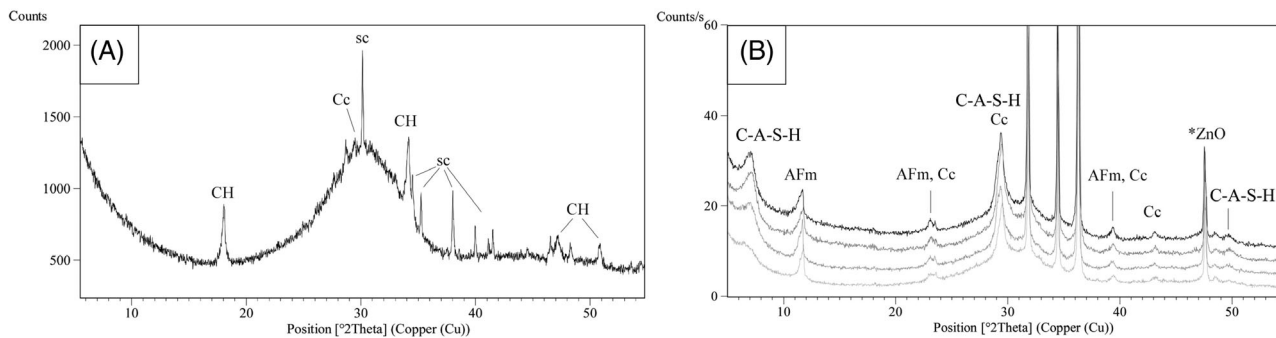


FIGURE 7 (A) Diffraction pattern of starting alkali-activated slag (AAS) dry powder. CH: portlandite; Cc: calcite; sc: sodium carbonate (natrite). (B) Diffraction patterns of pulverized aged AAS pastes ($w/s = 0.4$) at 1, 7, 14, and 150 days (from bottom to top) of curing time. ZnO: internal standard.

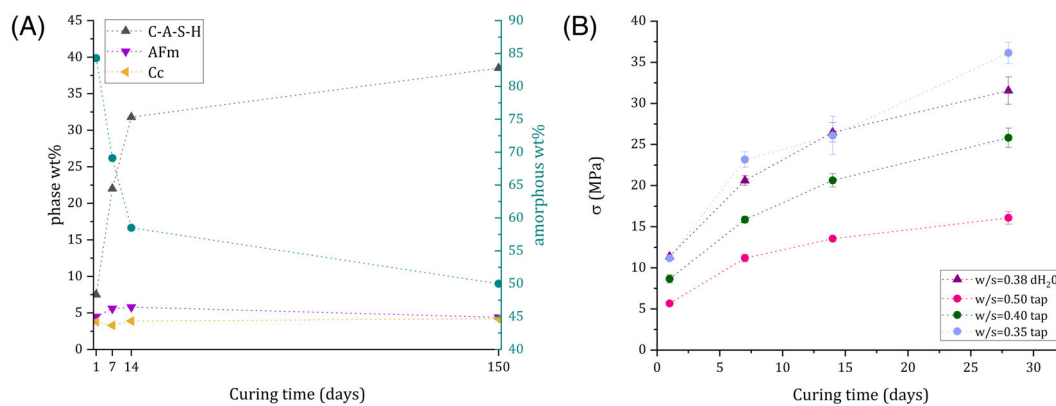


FIGURE 8 (A) Estimated weight fractions of nano-C-A-S-H, amorphous slag and crystalline phases in alkali-activated slag (AAS) pastes ($w/s = 0.4$) at increasing curing time. Error bars are smaller than symbols. (B) Mechanical compressive tests over time for AAS mortar prisms at different w/s .

(Figure S3). With respect to the early-hydration diffraction patterns shown in Figure 3, the nano-C-A-S-H diffraction features of Figure 7B are more evident due to the progressive structuration and growth of the nanocrystalline domains. In particular, the peak at $7^\circ 2\theta$ (corresponding to the evolution of the large hump at 0.4 \AA^{-1} observed in the S-XRPD pattern after 76 h, Figure 1D) shows the continuous structuration of nano-C-A-S-H along the c -axis, namely the progressive stacking of calcium-aluminosilicate layers of a tobermorite-like structure.

The sharp and intense peaks in Figure 7B are related to the internal standard zincite (ZnO). The wide hump around $30^\circ 2\theta$ is the contribution of the amorphous slag. The intensity of the nano-C-A-S-H peaks shows a significant increase as a function of the curing time, whereas peaks of AFm and calcite preserve their intensity throughout the investigated time interval. Quantitative phase analysis with the Rietveld and PONKCS methods allowed a direct quantification of nano-C-A-S-H in the paste at different curing times. The estimated weight fractions of nano-C-A-S-H (via Rietveld-PONKCS), amorphous slag

and crystalline phases (via internal standard ZnO) in pulverized aged AAS pastes ($w/s = 0.4$) are shown in Figure 8A. It should be noted that the weight fractions are calculated on the basis of the total mass of solids, which increases with the proceeding of hydration as free water is incorporated into the structure of the hydration products. The results of *mechanical testing* (i.e., compressive strengths σ) on the AAS mortar are also shown in Figure 8B. For each w/s , eight prisms ($2 \times 2 \times 8 \text{ cm}^3$) were tested at different curing times. All these samples are prepared with 30% (by volume) of standard sand (1–2 mm) and tap or distilled water.

The estimated weight fraction of nano-C-A-S-H in Figure 8A is less than 10% after 1 day, increases to 30% at 14 days, and then continues to grow more slowly over time. An inverse trend is observed for the amorphous content with an estimated weight fraction of 85% after 1 day which decreases to 60% at 14 days and 50% at 150 days. The content of AFm phases and calcite remains constant over the 150 days. The amount of calcite detected is close to the amount expected to precipitate from the reaction of the precursors,

with no further calcite formation. The amorphous fraction is mainly related to the slag and its decreasing content, coupled with the increase in nano-C-A-S-H, testifying to the advancement of the hydration process and the consequent increase in mechanical properties, as shown in Figure 8B for different AAS mortar prisms. As hydration progresses, the compressive strength σ of the mortar increases (for each w/s). Results show that all the tested samples, including the high w/s, achieve a compressive strength σ between 5 and 12 MPa after only 1 day. The best compressive strength is obtained (as expected) for the lowest w/s, reaching values suitable for low-bearing applications. The difference in strength observed from prisms prepared with distilled and tap water demonstrates a high sensitivity to the composition of the solution, indicating a lower robustness of AAS formulations compared to cement-based ones. In Figure S5, a direct comparison is made between tap and distilled water on the 28-day σ versus w/s.

Overall, the parallel between XRPD and mechanical tests clearly shows that the strength developed by the AAS mortar can be mainly attributed to the formation (and structuration) of nano-C-A-S-H, whose content is significant even after only 1 day.

4 | CONCLUSION

In this article, we provide a comprehensive characterization of a one-part AAS, activated with two solid powders (Na_2CO_3 and $\text{Ca}(\text{OH})_2$) at both early (≈ 1 min) and long-term (≈ 150 days) hydration times, focusing on its physico-chemical, rheological, and mechanical properties. Here, we devised a novel multiscale approach, taking advantage of the complementarity of different techniques, which were combined for the first time to link the structural and microstructural features of the paste to its rheological and mechanical behavior at the macroscale. The initial dissolution of the two activators and the precipitation of CaCO_3 are detected by pH and calorimetry. The fruitful combination of in situ XRPD and SAOS explains the mechanisms behind the early hydration evolution of the paste in the first hours. Both techniques show (for the same w/s = 0.6) an increase in reactivity in the first hour of the AAS paste directly linked to a strong increase in the early nano-C-A-S-H precipitation. SAOS was demonstrated to be a powerful tool for defining the initial reactivity of a complex paste and its workability limit (i.e., setting), as confirmed by Vicat for two w/s. This rapid early hydration was never observed, to the best of our knowledge, in similar one-part AAS. The long-term hydration properties are described by ex situ XRPD and mechanical testing. The increase in compressive strength σ of AAS mortar can be directly correlated with the increase

in nano-C-A-S-H (in pulverized aged AAS pastes), which is sufficient to develop adequate mechanical properties after one day (i.e., easily demoldable). These results provide practical information for the future use of less hazardous and more sustainable one-part AAS characterized by sufficient early reactivity (maintaining good workability under remixing), appropriate setting time, and rapid development of mechanical properties. Furthermore, here we highlight the relevance of this approach to the study of complex systems, such as AAS, that can be promptly transferred to the characterization of other binder formulations in terms of physico-chemical and mechanical properties, enabling their effective deployment.


ACKNOWLEDGMENTS


A.R. and T.L. thank Österreichische Bautechnik Vereinigung (ÖBV) and Österreichische Forschungsförderungsgesellschaft (FFG) for their support (project number: 870962). The authors also acknowledge TU Wien Bibliothek for financial support through its Open Access Funding Programme. G.D.S. and M.C.D. heartily acknowledge the scientific and technical staff at the X04SA-MS beamline of the Swiss Light Source (Paul Scherrer Institut, Villigen, CH).

ORCID

Teresa Liberto  <https://orcid.org/0000-0002-4985-9110>

Maria Chiara Dalconi  <https://orcid.org/0000-0001-8271-8929>

Gregorio Dal Sasso  <https://orcid.org/0000-0002-2176-5446>

Maurizio Bellotto  <https://orcid.org/0000-0002-3798-1098>

Agathe Robisson  <https://orcid.org/0000-0002-2434-6175>

REFERENCES

1. UN Environment, Scrivener KL, John VM, Gartner EM. Eco-efficient cements: potential economically viable solutions for a low- CO_2 cement-based materials industry. *Cem Concr Res*. 2018;114:2–26. <https://doi.org/10.1016/j.cemconres.2018.03.015>
2. Lombardi DR, Laybourn P. Redefining industrial symbiosis. *J Ind Ecol*. 2012;16(1):28–37. <https://doi.org/10.1111/j.1530-9290.2011.00444.x>
3. Palomo A, Maltseva O, Garcia-Lodeiro I, Fernández-Jiménez A. Portland versus alkaline cement: continuity or clean break: “a key decision for global sustainability”. *Front Chem*. 2021;9:705475.
4. Bernal SA, Provis JL. Durability of alkali-activated materials: progress and perspectives. *J Am Ceram Soc*. 2014;97(4):997–1008.
5. Provis JL. Alkali-activated materials. *Cem Concr Res*. 2018;114:40–8.
6. Pribulova A, Futáš P, Petřík J, Pokusová M, Brzeziński M, Jakubski J. Comparison of cupola furnace and blast furnace slags with respect to possibilities of their utilization. *Arch Metall Mater*. 2018;63(4):1865–73.

7. Bellotto MP, Zanelli SV, Brotto M. Process for producing a precursor for a hydraulic binder. EU Patent EP4089061A1. 2022.
8. Garcia-Lodeiro I, Palomo A, Fernández-Jiménez A. An overview of the chemistry of alkali-activated cement-based binders. Handbook of alkali-activated cements, mortars and concretes. Woodhead Publishing; 2015. p. 19–47.
9. Luukkonen T, Abdollahnejad Z, Yliniemi J, Kinnunen P, Illikainen M. One-part alkali-activated materials: a review. *Cem Concr Res*. 2018;103:21–34.
10. Segura IP, Luukkonen T, Yliniemi J, Sreenivasan H, Damø AJ, Jensen LS, et al. Comparison of one-part and two-part alkali-activated metakaolin and blast furnace slag. *J Sustain Metall*. 2022;8(4):1816–30.
11. Shi C, Roy D, Krivenko P. Alkali-activated cements and concretes. CRC Press; 2003.
12. Purdon AO. Improvements in processes of manufacturing cement, mortars and concretes. British Patent GB427. 1935. p. 227.
13. Myers RJ, Bernal SA, Provis JL. Phase diagrams for alkali-activated slag binders. *Cem Concr Res*. 2017;95:30–8.
14. Adesina A. Performance and sustainability overview of sodium carbonate activated slag materials cured at ambient temperature. *Resource Environ Sustain*. 2021;3:100016.
15. Bernal SA. Advances in near-neutral salts activation of blast furnace slags. *RILEM Tech Lett*. 2016;1:39–9.
16. Burciaga-Díaz O, Escalante-García JI. Structure, mechanisms of reaction, and strength of an alkali-activated blast-furnace slag. *J Am Ceram Soc*. 2013;96(12):3939–48.
17. Bernal SA, Nicolas RS, van Deventer JS, Provis JL. Alkali-activated slag cements produced with a blended sodium carbonate/sodium silicate activator. *Adv Cem Res*. 2016;28(4):262–73.
18. Jiao Z, Wang Y, Zheng W, Huang W. Effect of dosage of sodium carbonate on the strength and drying shrinkage of sodium hydroxide based alkali-activated slag paste. *Constr Build Mater*. 2018;179:11–24.
19. Awoyera P, Adesina A. A critical review on application of alkali activated slag as a sustainable composite binder. *Case Stud Constr Mater*. 2019;11:e00268.
20. Kovtun M, Kearsley EP, Shekhovtsova J. Dry powder alkali-activated slag cements. *Adv Cem Res*. 2015;27(8):447–56.
21. Yuan B, Yu Q, Brouwers H. Assessing the chemical involvement of limestone powder in sodium carbonate activated slag. *Mater Struct*. 2017;50:1–14.
22. Wang J, Lyu X, Wang L, Cao X, Liu Q, Zang H. Influence of the combination of calcium oxide and sodium carbonate on the hydration reactivity of alkali-activated slag binders. *J Cleaner Prod*. 2018;171:622–9.
23. Adesina A. Influence of various additives on the early age compressive strength of sodium carbonate activated slag composites: an overview. *J Mech Behav Mater*. 2020;29(1):106–13.
24. Burciaga-Díaz O, Betancourt-Castillo I, Montes-Escobedo M, Escalante-García J. One-part pastes and mortars of CaO–Na₂CO₃ activated blast furnace slag: microstructural evolution, cost and CO₂ emissions. *Constr Build Mater*. 2023;368:130431.
25. Atkins M, Bennett D, Dawes A, Glasser F, Kindness A, Read D. A thermodynamic model for blended cements. *Cem Concr Res*. 1992;22(2–3):497–502.
26. Lothenbach B, Gruskovnjak A. Hydration of alkali-activated slag: thermodynamic modelling. *Adv Cem Res*. 2007;19(2):81–92.
27. Lothenbach B. Thermodynamic equilibrium calculations in cementitious systems. *Mater Struct*. 2010;43(10):1413–33.
28. Myers RJ, Bernal SA, Provis JL. A thermodynamic model for C-(N-)ASH gel: CNASH_{ss}. Derivation and validation. *Cem Concr Res*. 2014;66:27–47.
29. Myers RJ, Lothenbach B, Bernal SA, Provis JL. Thermodynamic modelling of alkali-activated slag cements. *Appl Geochem*. 2015;61:233–47.
30. Fernández-Jiménez A, Puertas F, Sobrados I, Sanz J. Structure of calcium silicate hydrates formed in alkaline-activated slag: influence of the type of alkaline activator. *J Am Ceram Soc*. 2003;86(8):1389–94.
31. Kumar A, Walder BJ, Kunhi Mohamed A, Hofstetter A, Srinivasan B, Rossini AJ, et al. The atomic-level structure of cementitious calcium silicate hydrate. *J Phys Chem C*. 2017;121(32):17188–96. <https://doi.org/10.1021/acs.jpcc.7b02439>
32. Kunhi Mohamed A, Moutzouri P, Berruyer P, Walder BJ, Siramanont J, Harris M, et al. The atomic-level structure of cementitious calcium aluminate silicate hydrate. *J Am Ceram Soc*. 2020;142(25):11060–71. <https://doi.org/10.1021/jacs.0c02988>
33. Scrivener K, Snellings R, Lothenbach B, editors. A practical guide to microstructural analysis of cementitious materials. Vol 540. Boca Raton, FL, USA: CRC Press; 2016.
34. Van Deventer JS, Provis JL, Duxson P. Technical and commercial progress in the adoption of geopolymers. *Miner Eng*. 2012;29:89–104.
35. Krizan D, Zivanovic B. Effects of dosage and modulus of water glass on early hydration of alkali-slag cements. *Cem Concr Res*. 2002;32(8):1181–8.
36. Myers RJ, L'Hôpital E, Provis JL, Lothenbach B. Effect of temperature and aluminium on calcium (aluminosilicate) hydrate chemistry under equilibrium conditions. *Cem Concr Res*. 2015;68:83–93.
37. Myers RJ, Bernal SA, Gehman JD, Deventer vJS, Provis JL. The role of Al in cross-linking of alkali-activated slag cements. *J Am Ceram Soc*. 2015;98(3):996–1004.
38. Bernal SA, Provis JL, Myers RJ, San Nicolas R, Deventer vJS. Role of carbonates in the chemical evolution of sodium carbonate-activated slag binders. *Mater Struct*. 2015;48(3):517–29.
39. Ke X, Bernal SA, Provis JL. Controlling the reaction kinetics of sodium carbonate-activated slag cements using calcined layered double hydroxides. *Cem Concr Res*. 2016;81:24–37.
40. Pacheco-Torgal F, Labrincha J, Leonelli C, Palomo A, Chindaprasit P. Handbook of alkali-activated cements, mortars and concretes. Elsevier; 2014.
41. Puertas F, Varga C, Alonso M. Rheology of alkali-activated slag pastes. Effect of the nature and concentration of the activating solution. *Cem Concr Compos*. 2014;53:279–88.
42. Gong K, White CE. Time-dependent phase quantification and local structure analysis of hydroxide-activated slag via X-ray total scattering and molecular modeling. *Cem Concr Res*. 2022;151:106642.
43. Palacios M, Houst YF, Bowen P, Puertas F. Adsorption of superplasticizer admixtures on alkali-activated slag pastes. *Cem Concr Res*. 2009;39(8):670–7.
44. Palacios M, Puertas F. Effectiveness of mixing time on hardened properties of waterglass-activated slag pastes and mortars. *ACI Mater J*. 2011;108(1):73.

45. Liberto T, Bellotto M, Robisson A. Small oscillatory rheology and cementitious particle interactions. *Cem Concr Res.* 2022;157:106790.
46. Palacios M, Gismera S, Alonso MM, d'Espinose de Lacaillerie JB, Lothenbach B, Favier A, et al. Early reactivity of sodium silicate-activated slag pastes and its impact on rheological properties. *Cem Concr Res.* 2021;140:106302.
47. Habert G, De Lacaillerie JD, Roussel N. An environmental evaluation of geopolymer based concrete production: reviewing current research trends. *J Cleaner Prod.* 2011;19(11):1229–38.
48. Buchwald A, Vanooteghem M, Gruyaert E, Hilbig H, De Belie N. Purdocement: application of alkali-activated slag cement in Belgium in the 1950s. *Mater Struct.* 2015;48(1):501–11.
49. Bellotto M, Dalconi M, Contessi S, Garbin E, Artioli G. Formulation, performance, hydration and rheological behavior of 'just add water' slag-based binders. In: *Proceedings of the First International Conference on Innovation in Low-Carbon Cement and Concrete Technology.* 2019. p. 3–6.
50. Nachbaur L, Mutin J, Nonat A, Choplin L. Dynamic mode rheology of cement and tricalcium silicate pastes from mixing to setting. *Cem Concr Res.* 2001;31(2):183–92.
51. Bellotto M. Cement paste prior to setting: a rheological approach. *Cem Concr Res.* 2013;52:161–8.
52. Mostafa AM, Yahia A. New approach to assess build-up of cement-based suspensions. *Cem Concr Res.* 2016;85:174–82.
53. Yuan Q, Lu X, Khayat KH, Feys D, Shi C. Small amplitude oscillatory shear technique to evaluate structural build-up of cement paste. *Mater Struct.* 2017;50(2):1–12.
54. Ma S, Qian Y, Kawashima S. Experimental and modeling study on the non-linear structural build-up of fresh cement pastes incorporating viscosity modifying admixtures. *Cem Concr Res.* 2018;108:1–9.
55. Bogner A, Link J, Baum M, Mahlbacher M, Gil-Diaz T, Lützenkirchen J, et al. Early hydration and microstructure formation of Portland cement paste studied by oscillation rheology, isothermal calorimetry, 1H NMR relaxometry, conductance and SAXS. *Cem Concr Res.* 2020;130:105977.
56. Huang T, Yuan Q, Zuo S, Li B, Wu Q, Xie Y. Evaluation of microstructural changes in fresh cement paste using AC impedance spectroscopy vs. oscillation rheology and 1H NMR relaxometry. *Cem Concr Res.* 2021;149:106556.
57. Gartner E, Young J, Damidot D, Jawed I. Hydration of Portland cement. *Struct Perform Cem.* 2002;2:57–113.
58. Vernet C, Demoulian P, Hawthorn F. Mecanismes reactionnels de l'hydratation. In: *7th International Congress on the Chemistry of Cements.* Vol 2. 1980. p. 267–78.
59. Tamás FD. Electrical conductivity of cement pastes. *Cem Concr Res.* 1982;12(1):115–20.
60. Maximilien S, Péra J, Chabannet M. Study of the reactivity of clinkers by means of the conductometric test. *Cem Concr Res.* 1997;27(1):63–73.
61. Chae SR, Moon J, Yoon S, Bae S, Levitz P, Winarski R, et al. Advanced nanoscale characterization of cement based materials using X-ray synchrotron radiation: a review. *Int J Concr Struct Mater.* 2013;7(2):95–110.
62. Willmott P, Meister D, Leake S, Lange M, Bergamaschi A, Böge M, et al. The materials science beamline upgrade at the swiss light source. *J Synchrotron Radiat.* 2013;20(5):667–82.
63. Provis JL, Hajimohammadi A, White CE, Bernal SA, Myers RJ, Winarski RP, et al. Nanostructural characterization of geopolymers by advanced beamline techniques. *Cem Concr Compos.* 2013;36:56–64.
64. Dinnebier RE, Billinge SJL. *Powder diffraction: theory and practice.* The Royal Society of Chemistry; 2008.
65. Coelho AA. TOPAS and TOPAS-academic: an optimization program integrating computer algebra and crystallographic objects written in C++. *J Appl Crystallogr.* 2018;51(1):210–8.
66. Dinnebier RE, Billinge SJ. *Powder diffraction: theory and practice.* Royal Society of Chemistry; 2008.
67. Venkata Krishnan R, Jogeswararao G, Parthasarathy R, Premalatha S, Prabhakar Rao J, Gunasekaran G, et al. Development of a semi-adiabatic isoperibol solution calorimeter. *Rev Sci Instrum.* 2014;85(12):124904.
68. Vargas EF. Semiadiabatic (isoperibol) solution calorimetry. *Characterization of materials.* 2002. p. 1–11.
69. Brandštetr J, Polcer J, Krátký J, Holešinsky R, Havlica J. Possibilities of the use of isoperibolic calorimetry for assessing the hydration behavior of cementitious systems. *Cem Concr Res.* 2001;31(6):941–7.
70. Šiler P, Kolářová I, Novotný R, Másilko J, Pořízka J, Bednárek J, et al. Application of isothermal and isoperibolic calorimetry to assess the effect of zinc on cement hydration. *J Therm Anal Calorim.* 2018;133:27–40.
71. Liberto T, Le Merrer M, Barentin C, Bellotto M, Colombani J. Elasticity and yielding of a calcite paste: scaling laws in a dense colloidal suspension. *Soft Matter.* 2017;13(10):2014–23.
72. Bellotto M, Rebours B, Clause O, Lynch J, Bazin D, Elkaïm E. A reexamination of hydrotalcite crystal chemistry. *J Phys Chem.* 1996;100(20):8527–34.
73. Dal Sasso G, Dalconi MC, Ferrari G, Pedersen JS, Tamburini S, Bertolotti F, et al. An atomistic model describing the structure and morphology of Cu-doped CSH hardening accelerator nanoparticles. *Nanomaterials.* 2022;12(3):342.
74. Steins P, Poulesquen A, Diat O, Frizon F. Structural evolution during geopolymerization from an early age to consolidated material. *Langmuir.* 2012;28(22):8502–10.
75. Snyder KA, Feng X, Keen B, Mason TO. Estimating the electrical conductivity of cement paste pore solutions from OH⁻, K⁺ and Na⁺ concentrations. *Cem Concr Res.* 2003;33(6):793–8.
76. Wang P, Anderko A, Young RD. Modeling electrical conductivity in concentrated and mixed-solvent electrolyte solutions. *Ind Eng Chem Res.* 2004;43(25):8083–92.
77. Kellermeier M, Raiteri P, Berg JK, Kempter A, Gale JD, Gebauer D. Entropy drives calcium carbonate ion association. *ChemPhysChem.* 2016;17(21):3535–41.
78. Jansen D, Goetz-Neunhoeffer F, Lothenbach B, Neubauer J. The early hydration of ordinary Portland cement (OPC): an approach comparing measured heat flow with calculated heat flow from QXRD. *Cem Concr Res.* 2012;42(1):134–8.
79. Sollich P, Lequeux F, Hébraud P, Cates ME. Rheology of soft glassy materials. *Phys Rev Lett.* 1997;78(10):2020.
80. Bonacci F, Chateau X, Furst EM, Fusier J, Goyon J, Lemaître A. Contact and macroscopic ageing in colloidal suspensions. *Nat Mater.* 2020;19(7):775–80.
81. Taylor HF, editor. *Cement chemistry.* Vol 2. London: Thomas Telford; 1997.

SUPPORTING INFORMATION

Additional supporting information can be found online in the Supporting Information section at the end of this article.

How to cite this article: Liberto T, Dalconi MC, Dal Sasso G, Bellotto M, Robisson A. Structure–function relationship during the early and long-term hydration of one-part alkali-activated slag. *J Am Ceram Soc.* 2023;106:5187–5202.
<https://doi.org/10.1111/jace.19173>